nature nanotechnology

Article

https://doi.org/10.1038/s41565-023-01327-0

Giant orbital magnetic moments and paramagnetic shift in artificial relativistic atoms and molecules

Received: 30 June 2022

Accepted: 13 January 2023

Published online: 6 March 2023

Check for updates

Zhehao Ge[1,7], Sergey Slizovskiy[2,3,7], Peter Polizogopoulos[1], Toyanath Joshi[1], Takashi Taniguchi[4], Kenji Watanabe[5], David Lederman[1], Vladimir I. Fal'ko[2,3,6] ✉ & Jairo Velasco Jr[1] ✉

Materials such as graphene and topological insulators host massless Dirac fermions that enable the study of relativistic quantum phenomena. Single quantum dots and coupled quantum dots formed with massless Dirac fermions can be viewed as artificial relativistic atoms and molecules, respectively. Such structures offer a unique testbed to study atomic and molecular physics in the ultrarelativistic regime (particle speed close to the speed of light). Here we use a scanning tunnelling microscope to create and probe single and coupled electrostatically defined graphene quantum dots to unravel the magnetic-field responses of artificial relativistic nanostructures. We observe a giant orbital Zeeman splitting and orbital magnetic moment up to ~70 meV T^{-1} and ~600μ_B (μ_B, Bohr magneton) in single graphene quantum dots. For coupled graphene quantum dots, Aharonov–Bohm oscillations and a strong Van Vleck paramagnetic shift of ~20 meV T^{-2} are observed. Our findings provide fundamental insights into relativistic quantum dot states, which can be potentially leveraged for use in quantum information science.

Graphene is an ideal platform for studying relativistic quantum phenomena because it hosts massless Dirac fermions[1] and has high gate tunability. As a result, multiple relativistic quantum phenomena have been demonstrated with graphene such as Klein tunnelling[2,3] and atomic collapse[4,5]. Such phenomena are important not only for fundamental research but also for technological applications. For example, Klein tunnelling renders graphene p–n junctions highly transparent, which makes graphene an outstanding platform for electron optics applications such as negative refraction[6], Veselago lensing[7] and beam collimation[8,9].

Quantum dots (QDs) are often referred to as artificial atoms because of their atomic-like electronic structure[10,11]. They have been widely studied over the last 40 years in semiconductors and have provided immense fundamental insight[12–14]. Recently, the confinement of massless Dirac fermions in electrostatically defined QDs has been achieved in graphene[15–24] and topological insulators[25]. Different from semiconductor QDs formed with massive Schrödinger fermions, QDs populated by massless Dirac fermions can be viewed as artificial relativistic atoms, thus offering a unique opportunity to study atomic properties in the ultrarelativistic regime (particle speed close to the speed of light).

For such artificial relativistic atoms, the usual relationship between orbital magnetic moment ($\vec{\mu}$) and angular momentum ($\vec{L}$) for atomic states ($\vec{\mu} = g\mu_B\vec{L}/\hbar$, where μ_B is the Bohr magneton, $\hbar$ is the Dirac

[1]Department of Physics, University of California Santa Cruz, Santa Cruz, CA, USA. [2]Department of Physics and Astronomy, University of Manchester, Manchester, UK. [3]National Graphene Institute, University of Manchester, Booth Street East, Manchester, UK. [4]International Center for Materials Nanoarchitectonics and National Institute for Materials Science, Tsukuba, Japan. [5]Research Center for Functional Materials, National Institute for Materials Science, Tsukuba, Japan. [6]Henry Royce Institute for Advanced Materials, Manchester, UK. [7]These authors contributed equally: Zhehao Ge, Sergey Slizovskiy. ✉e-mail: Vladimir.Falko@manchester.ac.uk; jvelasc5@ucsc.edu

constant and g is the Landé g-factor) is invalid. This is because massless Dirac fermions disobey the non-relativistic relationship between velocity and momentum, namely, $\vec{p} = m\vec{v}$. Instead, $\vec{\mu}$ is given by the area of the atomic orbit (πr^2) multiplied by the electrical current ($\frac{-ev_D}{2\pi r}$), which results in $\vec{\mu} = -e\vec{v}_D \times \vec{r}/2$. Because of this, the large and constant Dirac velocity $\vec{v}_D$ together with a sizable atomic orbital radius $\vec{r}$ can produce extremely large $\vec{\mu}$ for artificial relativistic atoms. One direct consequence of this large $\vec{\mu}$ is a giant Zeeman splitting for artificial atomic orbital states in a magnetic field (B), which can potentially be useful for sensing. Such properties of artificial relativistic atoms, however, have not been experimentally demonstrated to date.

In this Article, we show B-dependent scanning tunnelling spectroscopy (STS) of gate-tunable single and coupled graphene quantum dots (GQDs) to unravel the unique B responses of artificial relativistic atoms and molecules. For single GQD states, we observed large linear splitting in B, which evidenced the giant $\vec{\mu}$ of these states. Next, we studied the angular quantum number and gate dependence of GQD $\vec{\mu}$ and found good agreement with theory. For coupled GQD states, we found that the linear splitting in B was quenched. Instead, a B^2-dependent energy shift towards lower energy was observed due to the existence of a strong paramagnetic shift in relativistic atomic systems. These phenomena underscore the uniqueness of GQDs compared with conventional semiconductor QDs.

Observation of linear orbital Zeeman splitting

We study GQDs defined by electrostatically induced circular p–n junctions with scanning tunnelling microscopy (STM) (Fig. 1a). Although Klein tunnelling[2,3] makes it difficult to confine massless Dirac fermions, their oblique incidence onto the circular p–n junction boundary (Fig. 1b) avoids the 100% transmission occurring at normal incidence. This allows for the formation of quasi-bound states in GQDs, which has been confirmed in previous experiments[15,17–21,23,24]. In zero B, the clockwise and counterclockwise quasi-bound states possessing the same radial quantum number (n) and angular quantum numbers ($\pm m$) are degenerate due to time-reversal symmetry. The directions of their $\vec{\mu}$, however, are opposite (Fig. 1c). Thus, by applying an external B, the degeneracy between the clockwise and counterclockwise quasi-bound states is lifted through an orbital Zeeman effect (Fig. 1d), leading to a splitting energy of $\Delta E = 2\left|\vec{\mu}\cdot\vec{B}\right|$. This linear orbital Zeeman splitting can be used to measure $\vec{\mu}$ of GQD states.

Importantly, the Berry-phase change in the GQD states[19,26] in B precludes the measurement of $\vec{\mu}$. To avoid this, we create GQDs with unprecedentedly sharp potential wells (Supplementary Section 2). Our method involves using a two-step tip-voltage-pulsing technique based on prior works[18,27] (Supplementary Section 3) on samples with reduced hexagonal boron nitride (hBN) thickness. Figure 1e shows a typical dI/dV_S spectra along a line across the centre of a circular p–n junction created with this technique on a large-angle (14.1°) twisted bilayer graphene (tBLG)/hBN sample. By tracking the graphene charge neutrality point (Fig. 1e, white dots), we estimate the potential variation to be ~200–300 meV across 100 nm. This is ~2–3 times sharper than previous works that utilized a related tip-voltage-pulsing technique[18,19,23,24]. Figure 1f shows a comparison of the dI/dV_S point spectra at $d = 0$ and 40 nm of the GQD shown in Fig. 1e. Evidently, the dI/dV_S peaks are much sharper off the centre than at the QD centre. This is because near the QD boundary, states with larger m are concentrated, which correspond to Dirac fermions propagating tangentially to the p–n junction, resulting in a stronger reflection and hence better confinement[17,18]. For the remainder of this work, we will focus on these large m states.

We now study the response of our GQDs to a perpendicular B. Figure 2a,b shows a comparison of $dI/dV_S(V_S, d)$ measured across the centre of another GQD with a sharp potential well under $B = 0$ and 0.2 T. Splitting patterns are clearly seen for $B = 0.2$ T as dimples near the QD boundary where high-m states concentrate. Figure 2c shows the evolution of the dI/dV_S point spectra at $d = 40$ nm for various B values; the splitting and merging of GQD states is evident as B increases. To visualize this behaviour more clearly, $dI/dV_S(V_S, B)$ with high B resolution was acquired (Fig. 2d). These data were taken from the GQD (Fig. 2a,b) at $d = 40$ nm; here $d^3I/dV_S^3(V_S, B)$ are presented to enhance the visibility of the dI/dV_S peaks (Extended Data Fig. 1 shows the raw $dI/dV_S(V_S, B)$ data). We observe a clear linear splitting for each QD state. We attribute this behaviour to orbital Zeeman splitting and find that it is present at locations off the QD centre but absent near the centre where low-m states concentrate (Supplementary Section 4). All these experimental findings are in good agreement with simulations based on a tight-binding (TB) model for a GQD (Supplementary Section 5) with a quadratic potential well (Fig. 2e–h), thus further supporting our qualitative understanding. The slight deviations visible between experiment and simulation at negative energies is probably due to the deviation in the experimental potential from the quadratic potential used in our simulation.

Angular quantum number and gate dependence of orbital magnetic moment

After confirming the existence of orbital Zeeman splitting, we now extract $\vec{\mu}$ of our artificial relativistic atom and study its angular quantum number and gate dependence. With spatially resolved dI/dV_S spectra (Fig. 2a,b), we can assign both radial and angular quantum numbers (n, m) for the GQD states in $d^3I/dV_S^3(V_S, B)$plots[19] (Supplementary Section 6); the assigned quantum numbers are shown in Fig. 2d,h. By using the simple consideration discussed in Fig. 1d ($\Delta E = 2\left|\vec{\mu}\cdot\vec{B}\right|$), the $\vec{\mu}$ value of the GQD states can then be extracted from the slopes of ΔE as a function of B. Figure 3a shows the extracted $\Delta E(B)$ and the corresponding linear fits for QD states with different m values at $V_G = -16$ V (Supplementary Section 7), a clear increase in slope is seen for states with larger m. The magnitude of $\vec{\mu}$ (μ) as a function of m extracted from the slopes of the linear fits (Fig. 3a) is plotted in Fig. 3b. An increase from $\sim 200\mu_B$ to $\sim 500\mu_B$ for μ is seen when m is increased from 2.5 to 10.5.

Next, we compare our experimentally extracted μ with theory. Approximately, the measured μ values are on the order of $\sim 300\mu_B$, which agrees well with the μ value of a current loop ($\mu = \frac{ev_F r}{2}$) for charge flowing with graphene's Fermi velocity $v_F = 10^6$ m s^{-1} and with a loop radius of $r = 35$ nm. For a more formal comparison, we calculated the m-resolved local density of states LDOS(E, B) from a continuum model for GQDs with quadratic potential wells (Supplementary Section 8); some results are shown in Fig. 3c–e. From such plots, we can extract μ for GQD states with different quantum numbers, and the extracted μ for states with $n = 0$ and $m = 2.5$–10.5 are plotted in Fig. 3b. Here we notice that the experimental results (red triangles) do not overlay any individual theory curve (empty circles). Additionally, the experimental results at larger m appear closer to the theoretical curves calculated with a smaller $|\kappa|$. Akin to the discrepancy shown in Fig. 2, the discrepancy evident here is probably caused by the deviation in the experimental potential from a quadratic potential at negative V_S (Extended Data Fig. 2). Nonetheless, for both experiment and theory, a clear increase in μ is seen with increasing m.

We now explore the gate dependence of μ for our artificial relativistic atoms. Figure 3f–h shows the $dI/dV_S(V_S, d)$ spectra measured at $V_G = -20$, -10 and 0 V and $B = 0.2$ T for the same QD in Fig. 2a. The potential-well sharpness of the GQDs in our experiments can be tuned by V_G (Supplementary Section 10). Apparently, as the potential-well sharpness increases with V_G, the splitting energy reduces. Figure 3i shows the experimentally extracted $\Delta E(B)$ for the $n = 0, m = 5.5$ QD state at various V_G values; the $d^3I/dV_S^3(V_S, B)$data at these V_G values are shown in Extended Data Fig. 3. A clear increase in slope is seen as V_G decreases, indicating an enhancement in μ as V_G reduces. To see this more quantitatively, we plot the extracted μ values as a function of m (Fig. 3j) for GQD states with different m values measured at various V_G values.

https://doi.org/10.1038/s41565-023-01327-0

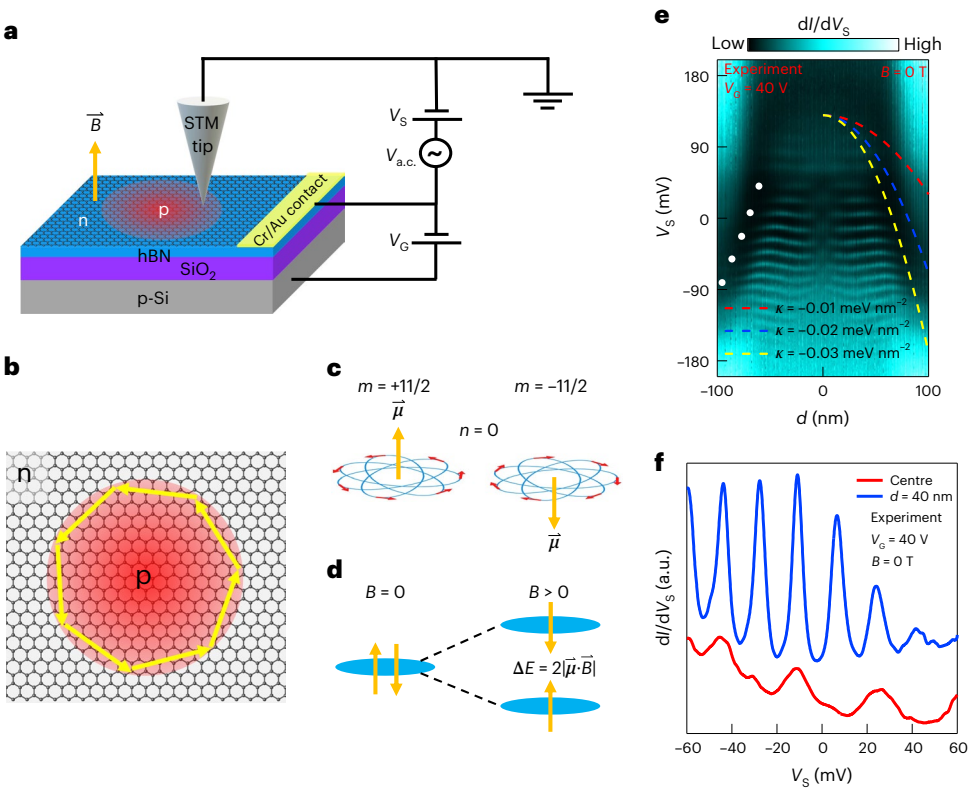

Fig. 1 | Experimental setup and orbital Zeeman splitting of GQD states. **a**, Schematic of the experimental setup. The circular graphene p–n junction is created in monolayer graphene or large-angle tBLG/hBN heterostructure (Supplementary Section 1) resting on a SiO_2/Si chip. The STM tip is grounded and a bias voltage V_S together with an a.c. voltage $V_{a.c.}$ is applied between the STM tip and graphene. A backgate voltage V_G is applied between the p-doped silicon and graphene and an out-of-plane magnetic field is applied to the whole device. **b**, Schematic of the confinement of massless Dirac fermions in a circular graphene p–n junction. **c**, Schematic of the orbital magnetic moments of GQD states. The blue lines are the calculated semiclassical orbits of $n = 0$, $m = \pm 11/2$ GQD states in a parabolic potential well $U(r) = -0.01r^2$ meV nm^{-2}. The red arrows indicate the direction of the trajectory. The orange arrows indicate the orientation of the orbital magnetic moments. **d**, Schematic of the orbital Zeeman splitting of GQD states in a finite magnetic field. The blue ovals and orange arrows represent the energy levels and orbital magnetic moment orientations of the GQD states, respectively. **e**, Experimentally measured $dI/dV_S(V_S, d)$ at $V_G = 0$ V along a line across the centre of a circular graphene p–n junction that has a sharp potential well. The coloured dashed lines are quadratic potential wells with different κ values. The set point used to acquire the tunnelling spectra was $I = 1$ nA, $V_S = -200$ mV and 2 mV a.c. modulation. **f**, The dI/dV_S point spectra at the centre and 40 nm away from the centre of the circular graphene p–n junction, as shown in **e**. The set point used to acquire the tunnelling spectra was $I = 1$ nA, $V_S = -60$ mV and 2 mV a.c. modulation.

The extracted μ values are generally smaller at larger V_G (sharper potential well) for all the QD states.

The observed gate tuning of μ can be understood as a result of orbital size tuning of the GQD states with V_G: sharper dots at larger V_G have current loops with a smaller radius. In contrast to non-relativistic atoms, μ for relativistic atoms is governed by the orbital radius instead of angular momentum. Therefore, it is uniquely possible to tune μ of our artificial relativistic atom by V_G and maintain the same quantum numbers. These results are also supported by the theoretically calculated $\mu(m)$ values for GQDs with different potential-well sharpness values (Fig. 3b).

We now compare the observed μ value in the GQDs with those of other systems. The value of μ observed in this work is orders of magnitude larger than those observed in natural atoms[28] and semiconductor QDs[29–31], and is also several times larger than that observed in Bernal-stacked bilayer graphene (BLG) QDs[32,33] (Table 1). Although similar μ values have been observed in Bernal-stacked trilayer graphene QDs[34], the findings in this work have several distinctions/advantages. Briefly, GQDs can achieve similar μ with a smaller QD size and maintain linear splitting within a larger B range compared with trilayer graphene QDs (Supplementary Section 11). Thus, the extremely large orbital Zeeman splitting observed in our GQDs (~23–58 meV T^{-1}) together with their nanometre-scale sizes offers a unique opportunity to fabricate magnetometer arrays with nanometre-scale spatial resolution (Supplementary Section 12). This is difficult to achieve for the current state of the art[35,36].

Coupled double GQDs

Having thoroughly investigated the μ values of single GQDs, below, we study the B response of coupled double GQDs, which can be viewed as artificial relativistic molecules[37]. These structures were created on a graphene/hBN sample by fabricating two circular p-doped regions with centres separated by 150 nm with our two-step tip-voltage-pulsing technique (Supplementary Section 3). Figure 4a shows a $d^3I/dV_S^3(V_S, d)$ plot measured along a line across the centres of two dots for $B = 0$ T at $V_G = 0$ V; the red and blue patterns in the plot correspond to dI/dV_S peaks and valleys, respectively. Three distinct regions can be identified (labelled as regions (i), (ii) and (iii) in Fig. 4a). In region (i), the energy spacing between the dI/dV_S peaks is half those in regions (ii) and (iii); in region (iii), different nodal patterns appear compared with region (ii). These features are distinct from uncoupled double GQDs made with a similar fabrication technique (Supplementary Section 12).

Next, we map the B response of our coupled GQDs. The plots of $d^3I/dV_S^3(V_S, B)$ measured in the three distinct regions of the coupled dots are shown in Fig. 4b–e. First, in region (i), we notice that the QD states display a positive energy shift that is proportional to B^2; such

https://doi.org/10.1038/s41565-023-01327-0

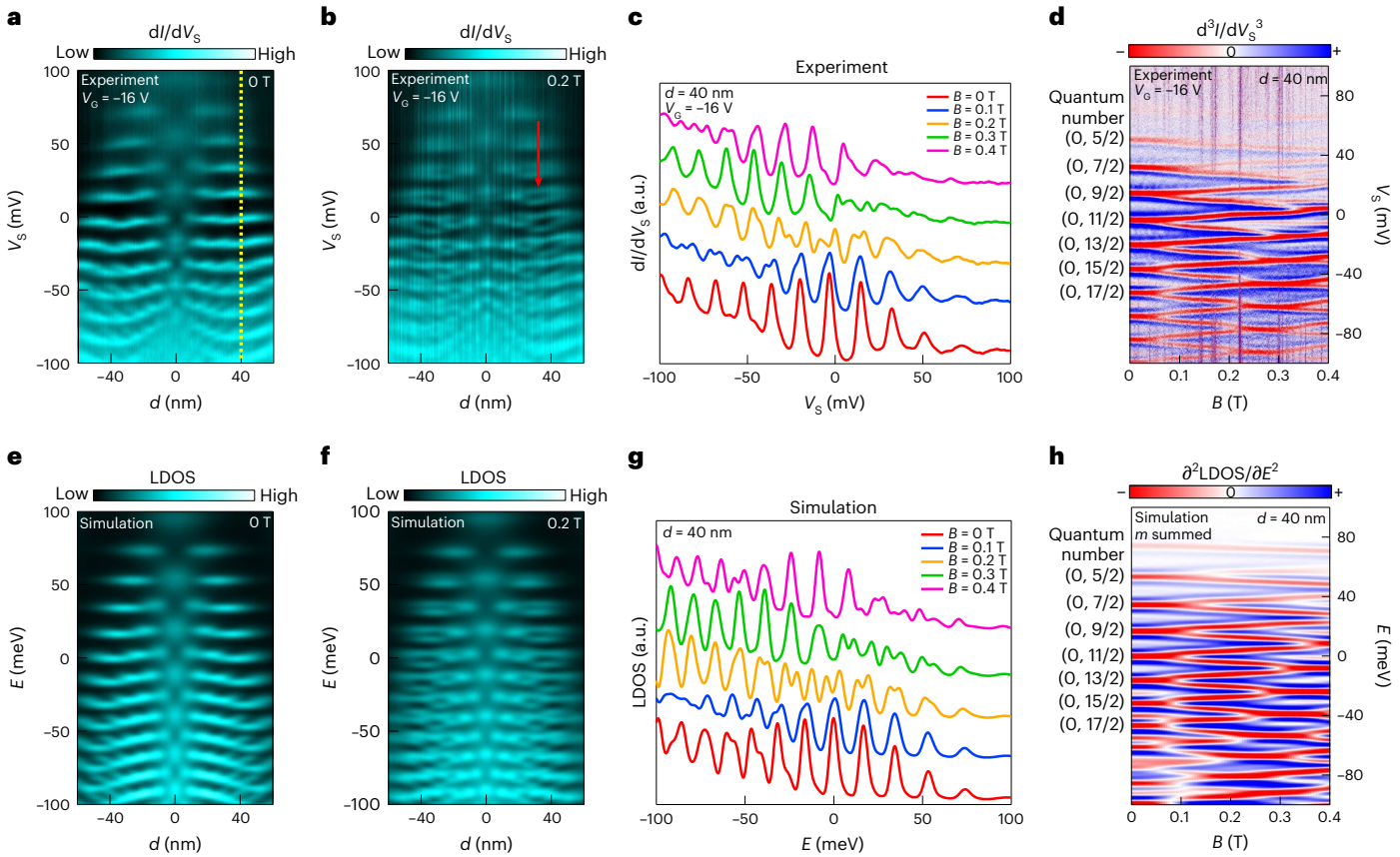

Fig. 2 | Experimental observation of linear orbital Zeeman splitting. **a**,**b**, Experimentally measured $dI/dV_S(V_S, d)$ at $V_G = -16$ V under $B = 0$ T (**a**) and $B = 0.2$ T (**b**) along a line across the centre of a circular graphene p–n junction with a sharp potential well. This p–n junction is different from the junction shown in Fig. 1e. The red arrow indicates the splitting of one QD state. **c**, The dI/dV_S point spectra measured at $d = 40$ nm and at $V_G = -16$ V under various magnetic fields from 0 to 0.4 T with a 0.1 T step. **d**, The $d^3I/dV_S^3(V_S, B)$ spectra at $V_G = -16$ V at $d = 40$ nm, as indicated by the yellow dashed lines in **a**. The quantum number (n, m) corresponds to the radial and angular quantum number, respectively. **e**,**f**, Simulated LDOS(E, d) for a GQD under $B = 0$ T (**e**) and $B = 0.2$ T (**f**) with $U(r) = -0.03r^2$ meV nm^{-2} + 160 meV. **g**, Simulated LDOS at $d = 40$ nm for various magnetic fields ranging from 0 to 0.4 T for the same GQD shown in **e** and **f**. **h**, Simulated $\partial^2\text{LDOS}/\partial E^2(E, B)$ at $d = 40$ nm for the same GQD shown in **e** and **f**.

behaviour is more evident in the zoomed-in view (Fig. 4c). The parabolic energy shift observed here is ~20 meV T^{-2}. Second, in region (ii), we encounter a linear splitting resembling the observation in single GQDs (Fig. 4d). Finally, region (iii) reveals a distinct behaviour compared with the other regions, namely, a staggered pattern for dI/dV_S peaks (Fig. 4e). All these observations are qualitatively reproduced with a TB model for a coupled double GQD (Supplementary Section 13).

To attain an intuitive understanding of these observations, we consider semiclassical orbits within strongly coupled double GQDs. For QD states in a single GQD, their semiclassical orbits can be approximated as circular orbits. Once these two QD states strongly couple, the circular orbits of individual QD states merge into a figure-eight orbit. A schematic of such an orbit indicated by yellow rings embedded in a double GQD is shown in Fig. 4f. Here the arrows indicate the reversed current-flow directions of the two rings with the figure-eight orbit. Note that the single-dot states with the same direction of circulation on the dot couple only weakly (for example, by potential gradient) due to the counterpropagation of states at the touching dot edges. Closer to each individual QD centre, we expect the QD states to have a smaller radius and are decoupled, thus forming circular orbits (Fig. 4f, green rings). In our experiment, regions (i) and (iii) correspond to QD states with figure-eight orbits and region (ii) corresponds to QD states with circular orbits. With this understanding in hand, the half-energy spacing observed in region (i) compared with region (ii) is due to the length of the figure-eight orbit being twice that of the circular orbit. This is because according to the semiclassical quantization rule, the energy spacing between the GQD states is $\Delta E = \frac{h v_F}{L}$, where h is the Planck constant, v_F is the graphene Fermi velocity and L is the semiclassical orbit length. Consequently, the large B-induced linear splitting observed in region (ii) can be explained by the large $\vec{\mu}$ value of the circular orbits akin to uncoupled GQDs.

Van Vleck paramagnetic shift and Aharonov-Bohm effect

We now discuss how the unique B response observed in region (i) corresponds to the emergence of a Van Vleck paramagnetic shift due to the relativistic nature of our artificial molecule. Because each of the two rings of the figure-eight orbit have reversed current-flow directions, their $\vec{\mu}$ are in opposite directions but with the same magnitude. Therefore, the net $\vec{\mu}$ value of an entire figure-eight orbit will be zero, thereby explaining the disappearance of linear splitting in B in regions (i) and (iii). Moreover, the positive parabolic energy shift for holes observed in region (i) is caused by a Van Vleck paramagnetic shift, which is a second-order perturbative B response[38]. Classically, this effect stems from a Lorentz force that expands (contracts) the orbits with μ aligned (anti-aligned) to B, resulting in an increase (decrease) in μ. The quenching of the first-order B effect in the figure-eight orbits helps the detection of this second-order effect. Importantly, for non-relativistic systems such as natural atoms[39] and semiconductor QDs[29,30,39], a Larmor diamagnetic shift due to the change in electron orbital velocity in B also exists and is usually stronger than the

https://doi.org/10.1038/s41565-023-01327-0

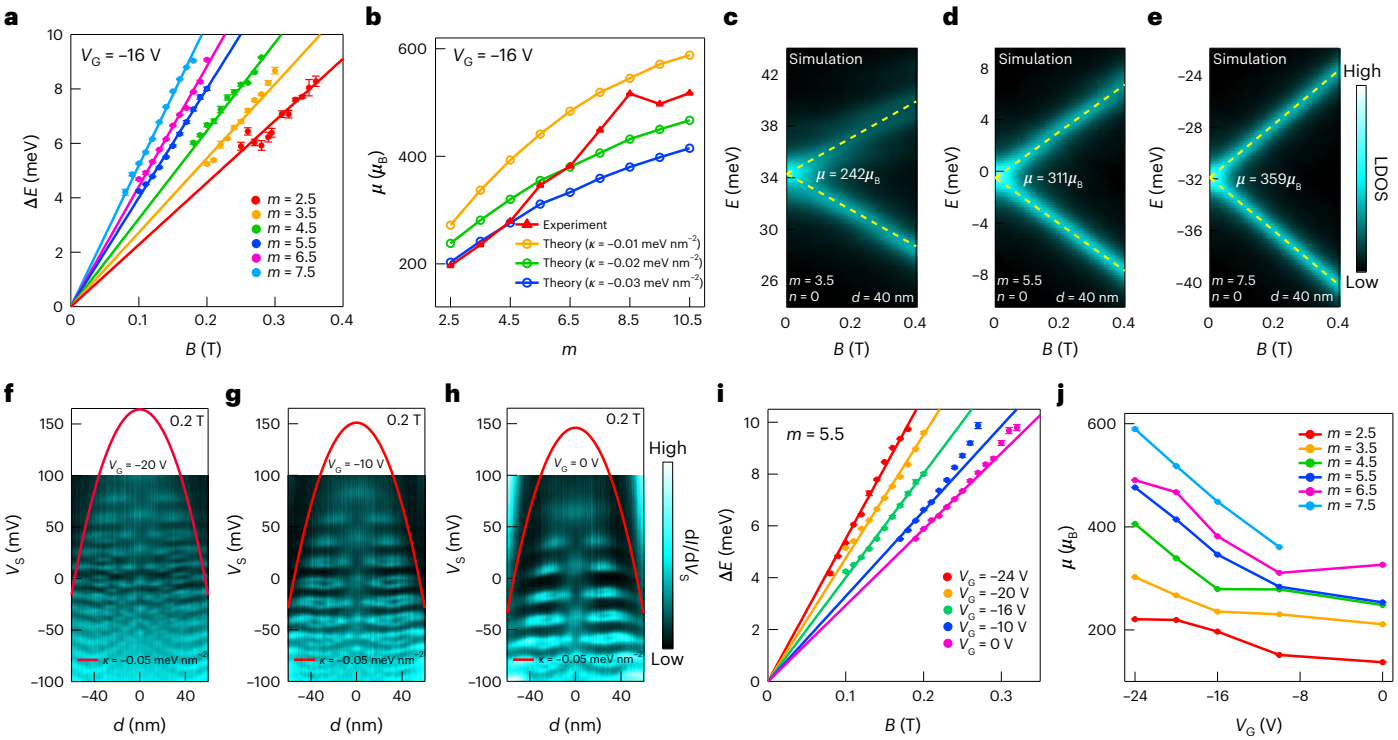

Fig. 3 | Quantum number and gate dependence of magnetic moments of GQD states. a, Experimentally extracted orbital Zeeman splitting energy at various B values and the linear fits for GQD states with different m values and $n = 0$ at $V_G = -16$ V. **b**, Comparison between experimentally extracted $\mu(m)$ at $V_G = -16$ V and theoretically calculated $\mu(m)$ for the GQD states with parabolic potential wells $U(r) = \kappa r^2$. **c**–**e**, Calculated m-resolved LDOS(E, B) at $d = 40$ nm for QD states with $n = 0$ and $m = 3.5$ (**c**), $m = 5.5$ (**d**) and $m = 7.5$ (**e**) in a GQD with $U(r) = -0.03r^2$ meV nm^{-2} + 160 meV. The yellow dashed lines indicate the theoretical orbital Zeeman splitting size with the μ value given in each plot. **f**–**h**, Experimentally measured $\mathrm{d}I/\mathrm{d}V_S(V_S, d)$ at $V_G = -20$ V (**f**), $V_G = -10$ V (**g**) and $V_G = 0$ V (**h**) at $B = 0.2$ T along a line across the centre of the same circular graphene p–n junction shown in Fig. 2a,b. The red curve in each plot represents a parabolic potential well with $\kappa = -0.05$ meV nm^{-2} and is a guide for the eye to aid a comparison between the potential-well sharpness variation for different V_G values. **i**, Experimentally extracted orbital Zeeman splitting energy at various B values and the corresponding linear fits for GQD states with $n = 0$, $m = 5.5$ at different V_G values. **j**, Experimentally extracted μ for the GQD states with different m values and $n = 0$ at different V_G values. The error bars in **a** and **i** reflect one standard error of the peak position in Gaussian multipeak fitting. The error bars in **b** and **j** reflect one standard error of the slope in weighted linear fitting (Supplementary Section 7).

Table 1 | Comparison of measured μ values for different types of system

System	Observed maximum effective μ
Natural atoms	On the order of several μ_B for their ground states and not highly excited states[28]
Self-assembled InP QDs[29]	~17.3μ_B (~2.0 meV T^{-1})
Self-assembled InAs/GaAs QDs[30]	~18.5μ_B (~2.1 meV T^{-1})
Self-assembled InAs/GaAs QDs[31]	~19.5μ_B (~2.3 meV T^{-1})
STM-tip-induced BLG QDs[32]	~86.0μ_B (~10.0 meV T^{-1})
Few-carrier BLG QDs[33]	~45.0μ_B (~5.0 meV T^{-1})
STM-tip-induced trilayer graphene QDs[34]	~525.0μ_B (~61.0 meV T^{-1})
This work (monolayer graphene QDs)	~600.0μ_B (~70.0 meV T^{-1})

For works in which the μ values are not directly given, we convert the observed Zeeman splitting ΔE in B to an effective μ through the definition $\mu = \frac{\Delta E}{2B}$.

Van Vleck paramagnetic shift. However, for GQDs, the Larmor diamagnetic shift is absent because of the constant velocity of massless Dirac fermions. Alternatively, this can be understood as resulting from the graphene Hamiltonian in B lacking a B^2 term that produces Larmor diamagnetism in non-relativistic systems (Supplementary Section 14). Such a B-induced response is thus unique to ultrarelativistic artificial atoms and molecules.

Finally, we discuss the origin of the staggered red stripe patterns in $\mathrm{d}^3I/\mathrm{d}V_S^3(V_S, B)$ plot in region (iii) and attribute them to Aharonov–Bohm (AB) oscillations occurring in region (iii). When a particle returns to its original position after travelling along a closed path, constructive (destructive) interference leading to enhanced (reduced) LDOS occurs if the action along the closed path $\frac{1}{\hbar}\oint \mathbf{p}\cdot \mathrm{d}\mathbf{q}$ equals to an even (odd) number of π. Here $\mathbf{p}$ and $\mathbf{q}$ are the canonical momentum and position coordinates, respectively. As shown in Fig. 4g, two distinct eigenenergies exist for the figure-eight orbits with constructive (yellow dot) and destructive (black dot) interference at the figure-eight orbit centre. This is because charges return to this location after travelling half of a figure-eight orbit. By applying an external B, the AB effect causes the pickup of additional phases ($\Delta\varphi = \frac{-e\Phi_B}{\hbar}$, where Φ_B is the magnetic flux through each circular segment) with opposite signs for the two circular orbits flowing in opposite directions. As a result, the energy level of the figure-eight orbit does not change in B to the first order, but the interference type at the figure-eight orbit centre switches depending on the amount of $\Delta\varphi$ picked up by each circular segment (Fig. 4g). This explains the staggered pattern observed in region (iii) (Fig. 4e), where the red and blue stripes (corresponding to constructive and destructive interference, respectively) alternate at a constant V_S in B. In addition, the assigned $\Delta\varphi$ values (Fig. 4e) are in good agreement with our

https://doi.org/10.1038/s41565-023-01327-0

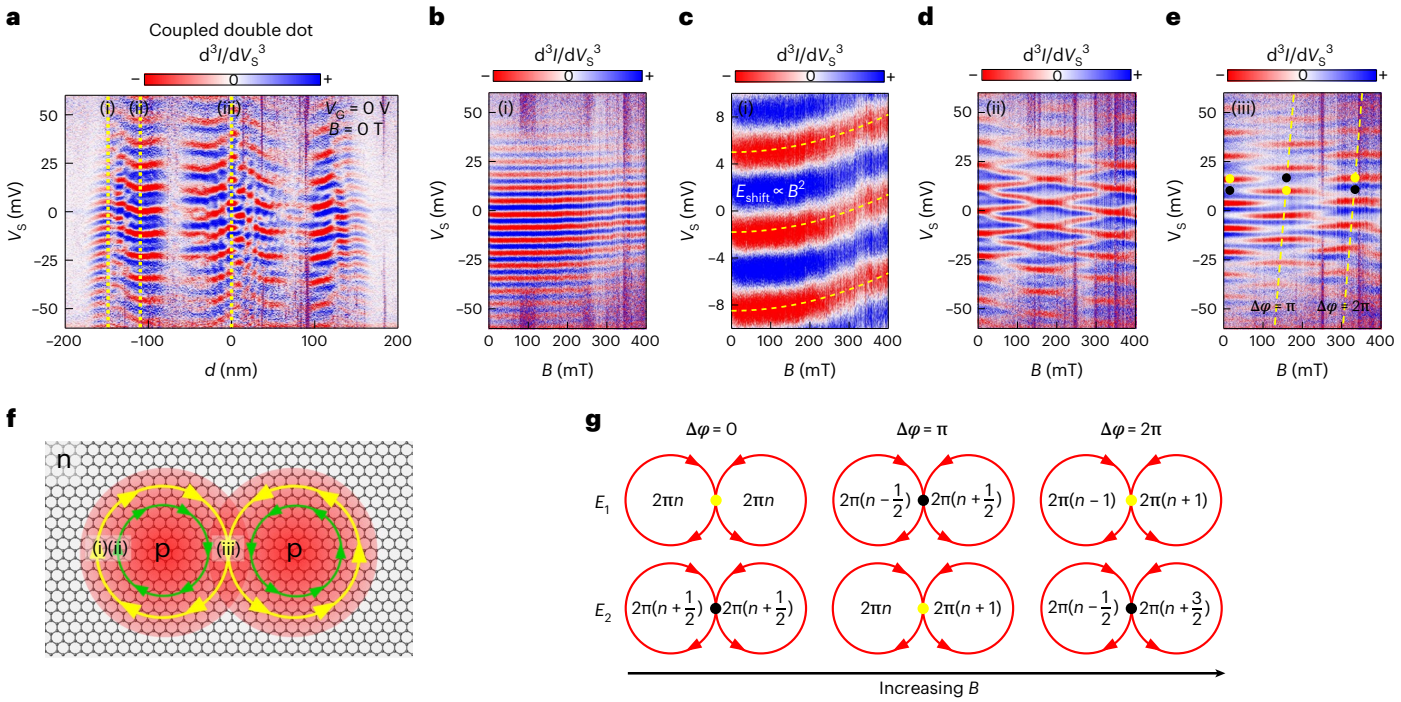

Fig. 4 | Paramagnetic shift and AB effect in coupled double GQDs. **a**, Experimentally measured $d^3I/dV_S^3(V_S, d)$ at $V_G = 0$ V and $B = 0$ T for coupled double GQDs that are separated by 150 nm. **b**, The $d^3I/dV_S^3(V_S, B)$ data measured at $V_G = 0$ V and $d = -110$ nm corresponding to region (i) in **a**. **c**, Zoomed-in view of **b** around $V_S = 0$. **d**, The $d^3I/dV_S^3(V_S, B)$ data measured at $V_G = 0$ V and $d = -110$ nm corresponding to region (ii) in **a**. **e**, The $d^3I/dV_S^3(V_S, B)$ data measured at $V_G = 0$ V and $d = 0$ nm corresponding to region (iii) in **a**. The yellow dashed lines indicate the approximate value of B at which the circular orbits pick up an integer number of π AB phase. The d^3I/dV_S^3 values in **a**–**e** were numerically calculated from the dI/dV_S data acquired through a lock-in measurement. The set point used to acquire the tunnelling spectra in **a**–**e** was $I = 1$ nA, $V_S = -60$ mV and 2 mV ac modulation. **f**, Schematic of the coupled double GQD, and the figure-eight and circular orbits; a degenerate time-reversed figure-eight orbit also exists, but it is not shown here for clarity. **g**, Schematic of the constructive (yellow dot) and destructive (black dot) interference at the centre of the figure-eight orbit for different energy levels and its tuning by B through the AB effect.

experimental double-dot geometry (Supplementary Section 15). This observed AB oscillation in the LDOS intensity of coupled GQDs can also be potentially used for B sensing.

Conclusions

We observed giant $\vec{\mu}$ and large orbital Zeeman splitting in artificial relativistic atoms formed with single GQDs. We also observed strong Van Vleck paramagnetic shifts and AB oscillations in artificial relativistic molecules formed with coupled double GQDs. These phenomena stem from the long-lived states near the GQD edges, thus resembling persistent currents in metallic rings[40,41]. Notably, our work demonstrates the potential for realizing giant and tunable persistent currents in GQDs. Such currents can potentially be used in quantum information processing[42] and quantum simulation[43].

Online content

Any methods, additional references, Nature Portfolio reporting summaries, source data, extended data, supplementary information, acknowledgements, peer review information; details of author contributions and competing interests; and statements of data and code availability are available at https://doi.org/10.1038/s41565-023-01327-0.

References

1. Novoselov, K. S. et al. Two-dimensional gas of massless Dirac fermions in graphene. *Nature* **438**, 197–200 (2005).
2. Katsnelson, M., Novoselov, K. & Geim, A. Chiral tunnelling and the Klein paradox in graphene. *Nat. Phys.* **2**, 620–625 (2006).
3. Young, A. F. & Kim, P. Quantum interference and Klein tunnelling in graphene heterojunctions. *Nat. Phys.* **5**, 222–226 (2009).
4. Wang, Y. et al. Observing atomic collapse resonances in artificial nuclei on graphene. *Science* **340**, 734–737 (2013).
5. Lu, J. et al. Frustrated supercritical collapse in tunable charge arrays on graphene. *Nat. Commun.* **10**, 477 (2019).
6. Chen, S. et al. Electron optics with p-n junctions in ballistic graphene. *Science* **353**, 1522–1525 (2016).
7. Cheianov, V. V., Fal'ko, V. & Altshuler, B. The focusing of electron flow and a Veselago lens in graphene p-n junctions. *Science* **315**, 1252–1255 (2007).
8. Cheianov, V. V. & Fal'ko, V. I. Selective transmission of Dirac electrons and ballistic magnetoresistance of n–p junctions in graphene. *Phys. Rev. B* **74**, 041403 (2006).
9. Liu, M.-H., Gorini, C. & Richter, K. Creating and steering highly directional electron beams in graphene. *Phys. Rev. Lett.* **118**, 066801 (2017).
10. Chakraborty, T. *Quantum Dots: A Survey of the Properties of Artificial Atoms* (Elsevier, 1999).
11. Reimann, S. M. & Manninen, M. Electronic structure of quantum dots. *Rev. Mod. Phys.* **74**, 1283 (2002).
12. Kouwenhoven, L. P., Austing, D. & Tarucha, S. Few-electron quantum dots. *Rep. Prog. Phys.* **64**, 701 (2001).
13. Hanson, R., Kouwenhoven, L. P., Petta, J. R., Tarucha, S. & Vandersypen, L. M. Spins in few-electron quantum dots. *Rev. Mod. Phys.* **79**, 1217 (2007).
14. Lodahl, P., Mahmoodian, S. & Stobbe, S. Interfacing single photons and single quantum dots with photonic nanostructures. *Rev. Mod. Phys.* **87**, 347 (2015).
15. Zhao, Y. et al. Creating and probing electron whispering-gallery modes in graphene. *Science* **348**, 672–675 (2015).

16. Freitag, N. M. et al. Electrostatically confined monolayer graphene quantum dots with orbital and valley splittings. *Nano Lett.* **16**, 5798–5805 (2016).
17. Gutiérrez, C., Brown, L., Kim, C.-J., Park, J. & Pasupathy, A. N. Klein tunnelling and electron trapping in nanometre-scale graphene quantum dots. *Nat. Phys.* **12**, 1069–1075 (2016).
18. Lee, J. et al. Imaging electrostatically confined Dirac fermions in graphene quantum dots. *Nat. Phys.* **12**, 1032–1036 (2016).
19. Ghahari, F. et al. An on/off Berry phase switch in circular graphene resonators. *Science* **356**, 845–849 (2017).
20. Jiang, Y. et al. Tuning a circular p–n junction in graphene from quantum confinement to optical guiding. *Nat. Nanotechnol.* **12**, 1045–1049 (2017).
21. Bai, K.-K. et al. Generating atomically sharp p–n junctions in graphene and testing quantum electron optics on the nanoscale. *Phys. Rev. B* **97**, 045413 (2018).
22. Freitag, N. M. et al. Large tunable valley splitting in edge-free graphene quantum dots on boron nitride. *Nat. Nanotechnol.* **13**, 392–397 (2018).
23. Quezada-López, E. A. et al. Comprehensive electrostatic modeling of exposed quantum dots in graphene/hexagonal boron nitride heterostructures. *Nanomaterials* **10**, 1154 (2020).
24. Behn, W. A. et al. Measuring and tuning the potential landscape of electrostatically defined quantum dots in graphene. *Nano Lett.* **21**, 5013–5020 (2021).
25. Zhang, J., Jiang, Y.-P., Ma, X.-C. & Xue, Q.-K. Berry-phase switch in electrostatically confined topological surface states. *Phys. Rev. Lett.* **128**, 126402 (2022).
26. Rodriguez-Nieva, J. F. & Levitov, L. S. Berry phase jumps and giant nonreciprocity in Dirac quantum dots. *Phys. Rev. B* **94**, 235406 (2016).
27. Ge, Z. et al. Visualization and manipulation of bilayer graphene quantum dots with broken rotational symmetry and nontrivial topology. *Nano Lett.* **20**, 8682–8688 (2020).
28. Bethe, H. A. & Salpeter, E. E. *Quantum Mechanics of One- and Two-Electron Atoms* (Springer Science & Business Media, 2012).
29. Rinaldi, R. et al. Zeeman effect in parabolic quantum dots. *Phys. Rev. Lett.* **77**, 342 (1996).
30. Paskov, P. et al. Magnetoluminescence of highly excited InAs/GaAs self-assembled quantum dots. *Phys. Rev. B* **62**, 7344 (2000).
31. Raymond, S. et al. Excitonic energy shell structure of self-assembled InGaAs/GaAs quantum dots. *Phys. Rev. Lett.* **92**, 187402 (2004).
32. Ren, Y.-N., Cheng, Q., Sun, Q.-F. & He, L. Realizing valley-polarized energy spectra in bilayer graphene quantum dots via continuously tunable Berry phases. *Phys. Rev. Lett.* **128**, 206805 (2022).
33. Tong, C. et al. Tunable valley splitting and bipolar operation in graphene quantum dots. *Nano Lett.* **21**, 1068–1073 (2021).
34. Ge, Z. et al. Control of giant topological magnetic moment and valley splitting in trilayer graphene. *Phys. Rev. Lett.* **127**, 136402 (2021).
35. Lenz, J. & Edelstein, S. Magnetic sensors and their applications. *IEEE Sens. J.* **6**, 631–649 (2006).
36. Degen, C. L., Reinhard, F. & Cappellaro, P. Quantum sensing. *Rev. Mod. Phys.* **89**, 035002 (2017).
37. Fu, Z.-Q. et al. Relativistic artificial molecules realized by two coupled graphene quantum dots. *Nano Lett.* **20**, 6738–6743 (2020).
38. Ashcroft, N. W. & Mermin, N. D. *Solid State Physics* (Cengage Learning, 1976).
39. Arimondo, E., Ciampini, D. & Rizzo, C. Chapter one—spectroscopy of natural and artificial atoms in magnetic fields. In *Advances In Atomic, Molecular, and Optical Physics* **65**, 1–66 (Elsevier, 2016).
40. Ambegaokar, V. & Eckern, U. Coherence and persistent currents in mesoscopic rings. *Phys. Rev. Lett.* **65**, 381 (1990).
41. Bleszynski-Jayich, A. et al. Persistent currents in normal metal rings. *Science* **326**, 272–275 (2009).
42. Mooij, J. et al. Josephson persistent-current qubit. *Science* **285**, 1036–1039 (1999).
43. Nisoli, C., Moessner, R. & Schiffer, P. Colloquium: artificial spin ice: designing and imaging magnetic frustration. *Rev. Mod. Phys.* **85**, 1473 (2013).

Methods

Sample fabrication

The graphene/hBN and tBLG/hBN samples were assembled with a standard polymer-based transfer method[44]. For the graphene/hBN sample, a graphene flake exfoliated on a methyl methacrylate (MMA) substrate was mechanically placed on top of an ~20-nm-thick hBN flake that rests on a 285 nm SiO_2/Si^{++} substrate. For the tBLG sample, we first use a monolayer graphene flake on MMA to pick up another monolayer graphene flake on the SiO_2/Si^{++} substrate and then we place tBLG/MMA onto an ~20-nm-thick hBN flake that rests on a 285 nm SiO_2/Si^{++} substrate. For both samples, the MMA scaffold was dissolved in a subsequent solvent bath. The assembled heterostructure is then annealed in forming gas (Ar/H_2) for ~12 h at 400 °C to reduce the residual polymer after the heterostructure assembly procedure. Next, an electrical contact to the sample is made by thermally evaporating 7 nm Cr and 200 nm Au using a metallic stencil mask. To further improve the sample surface cleanliness, the heterostructure is then mechanically cleaned using an atomic force microscope[45], which is done in a glovebox filled with N_2 gas. We perform sequential scans in the contact mode (set point, 0.2 V; scanning speed, ~15 μm s^{-1}; resolution, 1,024 × 1,024 pixels) to sweep regions of ~30 × 30 μm^2 by a Cypher S atomic force microscope with Econo-ESP-Au tips from Oxford Instruments. Finally, the heterostructure is annealed in an ultrahigh vacuum at 400 °C for 7 h before being introduced into the STM chamber.

STM/STS measurements

The STM/STS measurements were conducted in an ultrahigh vacuum with pressures higher than 1×10^{-10} mbar at 4.8 K in a Createc LT-STM instrument. Electrochemically etched tungsten tips calibrated on a Au(111) surface were used in the experiments. The lock-in a.c. signal frequency used for the STS measurements was 704 Hz.

Data availability

Source data are provided with this paper. Any additional material is available from the corresponding authors upon reasonable request.

Code availability

All the codes used in this Article are available from the corresponding authors upon request.

References

44. Zomer, P., Dash, S., Tombros, N. & Van Wees, B. A transfer technique for high mobility graphene devices on commercially available hexagonal boron nitride. *Appl. Phys. Lett.* **99**, 232104 (2011).
45. Goossens, A. et al. Mechanical cleaning of graphene. *Appl. Phys. Lett.* **100**, 073110 (2012).

Acknowledgements

We thank the Hummingbird Computational Cluster team at University of California Santa Cruz for providing computational resources for the numerical TB calculations performed in this work, and M. Hance for providing insight into the accelerator physics considerations related to our experimental findings. J.V.J. and Z.G. acknowledge support from the National Science Foundation under award DMR-1753367. J.V.J. acknowledges support from the Army Research Office under contract W911NF-17-1-0473. V.I.F. and S.S. acknowledge support from the European Graphene Flagship Core 3 Project. V.I.F. acknowledges support from the Lloyd Register Foundation Nanotechnology Grant and EPSRC grants EP/V007033/1, EP/S030719/1 and EP/N010345/1. K.W. and T.T. acknowledge support from the Elemental Strategy Initiative conducted by the MEXT, Japan, via grant no. JPMXP0112101001 and JSPS KAKENHI via grant no. JP20H00354.

Author contributions

Z.G. and J.V.J. conceived the work and designed the research strategy. Z.G. fabricated the samples and performed the data analysis under the supervision of J.V.J. K.W. and T.T. provided the hBN crystals. Z.G. carried out the tunnelling spectroscopy measurements with assistance from P.P. and T.J. under the supervision of D.L. and J.V.J. S.S. developed the interpretation for experimental findings and performed the continuum model calculations under the supervision of V.I.F. Z.G. performed the numerical TB calculations with input from S.S. under the supervision of V.I.F. and J.VJ. Z.G. and J.V.J. wrote the paper. All the authors discussed the paper and commented on the manuscript.

Competing interests

The authors declare no competing interests.

Additional information

Extended data is available for this paper at https://doi.org/10.1038/s41565-023-01327-0.

Supplementary information The online version contains supplementary material available at https://doi.org/10.1038/s41565-023-01327-0.

Correspondence and requests for materials should be addressed to Vladimir I. Fal'ko or Jairo Velasco.

Peer review information *Nature Nanotechnology* thanks the anonymous reviewers for their contribution to the peer review of this work.

https://doi.org/10.1038/s41565-023-01327-0

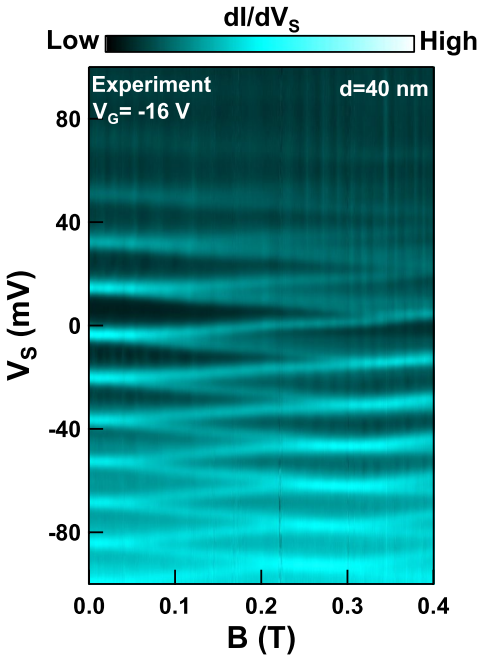

Extended Data Fig. 1 | Raw $dI/dV_S(V_S, B)$ used to get $d^3I/dV_S^3(V_S, B)$ plot in Fig. 2d. dI/dV_S (V_S, B) taken at d = 40 nm for the same GQD shown in Fig. 2a,b at V_G = −16 V. The set point used to acquire the tunneling spectra was I = 1 nA, V_S = −60 mV, with a 2 mV ac modulation.

https://doi.org/10.1038/s41565-023-01327-0

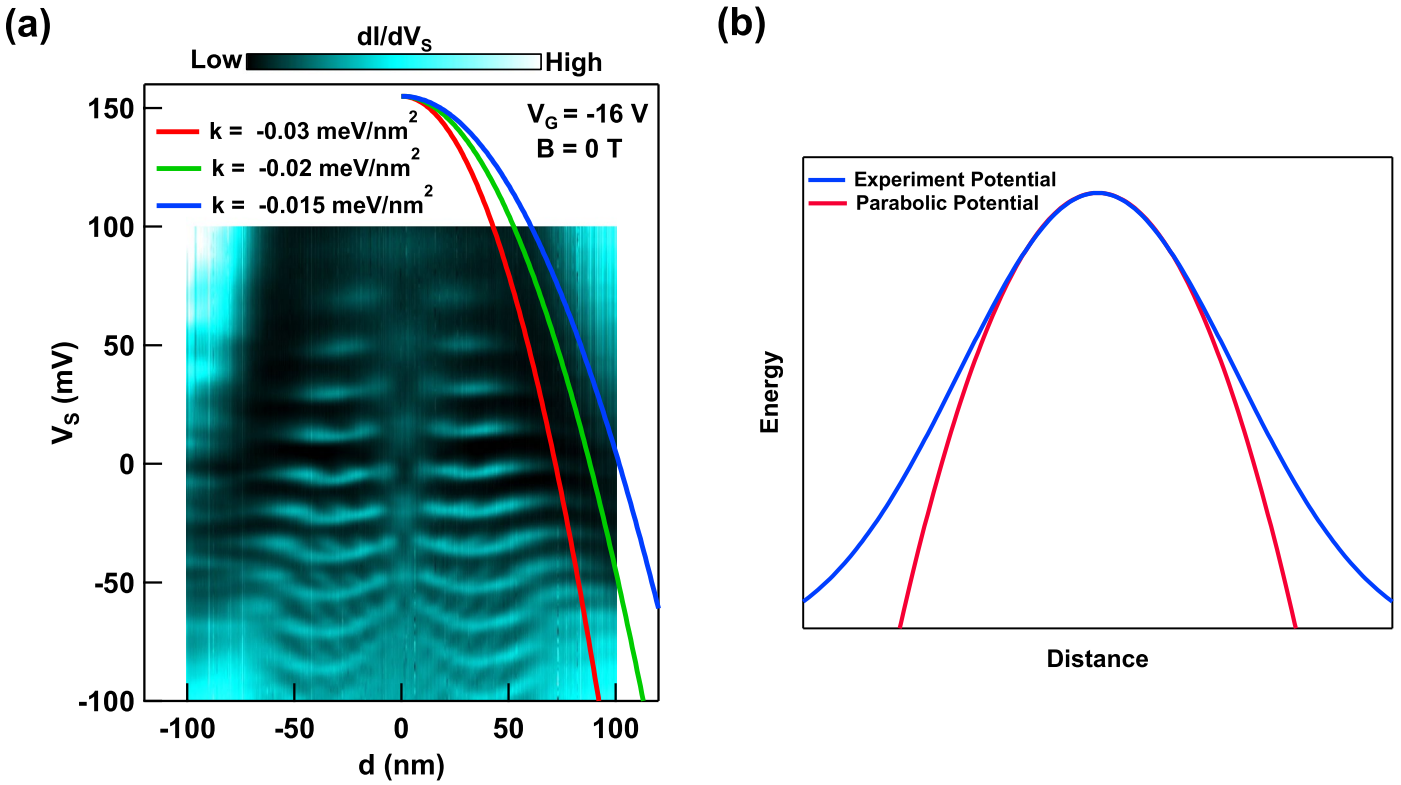

Extended Data Fig. 2 | Deviation between experimental potential well and parabolic potential well. a, Experimentally measured dI/dV_S (V_S, d) for the same QD shown in Fig. 2a at $V_G = -16$ V along a line across the center of a circular graphene pn junction. Colored lines are quadratic potential wells with different κ values. The set point used to acquire the tunneling spectra was $I = 1$ nA, $V_S = -200$ mV, with a 2 mV ac modulation. **b**, Schematic of the deviation between experimental potential well and parabolic potential well at more negative energies. The experimental potential well deviates from parabolic potential well at more negative energies, and the actual QD radius will be larger than the parabolic potential well. This explains the faster increase of experimentally measured μ than the theoretical values for graphene QDs with a quadratic potential well.

https://doi.org/10.1038/s41565-023-01327-0

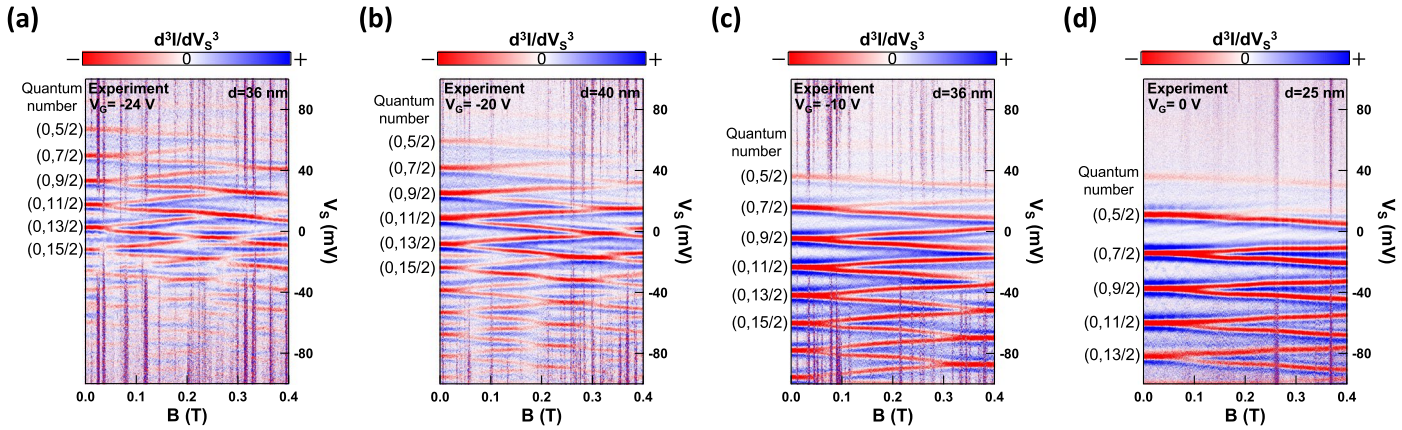

Extended Data Fig. 3 | $d^3I/dV_S^3(V_S, B)$ plot at different V_G. **a**, $d^3I/dV_S^3(V_S, B)$ at $V_G = -24$ V and at $d = 36$ nm. **b**, $d^3I/dV_S^3(V_S, B)$ at $V_G = -20$ V and at $d = 40$ nm. **c**, $d^3I/dV_S^3(V_S, B)$ at $V_G = -10$ V and at $d = 36$ nm. **d**, $d^3I/dV_S^3(V_S, B)$ at $V_G = 0$ V and at $d = 25$ nm. The quantum number (n,m) in (a–d) corresponds to radial and angular quantum number, respectively.